



Influence of hexagonal to orthorhombic phase transformation on diffusion-controlled dendrite evolution in directionally solidified Sn–Ni peritectic alloy

Peng PENG^{1,2}, Bi-zhou ZHAO³, Jia-tai WANG², Xing PEI¹, Zi-jie LIU¹, Lu GAN¹, Sheng-yuan LI¹

1. School of Materials and Energy, Lanzhou University, Lanzhou 730000, China;

2. School of Physics and Electronic Information Engineering, Qinghai Normal University, Xining 753000, China;

3. Gansu Provincial Hospital of Traditional Chinese Medicine, Lanzhou 730000, China

Received 30 April 2021; accepted 24 December 2021

Abstract: The hexagonal to orthorhombic (HO) transformation from β -Ni₃Sn₂ (hexagonal) phase to α' -Ni₃Sn₂ (orthorhombic) phase was confirmed in directionally solidified Sn–Ni peritectic alloys. It is shown that the remelting/resolidification process which is caused by both the temperature gradient zone melting (TGZM) and Gibbs–Thomson (G–T) effects can take place on secondary dendrites. Besides, the intersection angle between the primary dendrite stem and secondary branch (θ) is found to increase from $\pi/3$ to $\pi/2$ as the solidification proceeds. This is the morphological feature of the HO transformation, which can change the diffusion distance of the remelting/resolidification process. Thus, a diffusion-based analytical model is established to describe this process through the specific surface area (S_V) of dendrites. The theoretical prediction demonstrates that the remelting/resolidification process is restricted when the HO transformation occurs during peritectic solidification. In addition, the slope of the prediction curves is changed, indicating the variation of the local remelting/resolidification rates.

Key words: directional solidification; dendritic solidification; peritectic microstructures; Gibbs–Thomson effect; temperature gradient zone melting; HO transformation

1 Introduction

The secondary dendrite arm is considered to be the most visually prominent feature of dendritic structures [1–7]. It has been confirmed in numerous works that different kinds of diffusion-controlled remelting/resolidification processes could take place on secondary dendrite arm in the mushy zone [8–20]. The most familiar one of these remelting/resolidification processes is coarsening process by Gibbs–Thomson (G–T) effect [8–11]. During dendritic solidification, the G–T effect can induce capillary-driven diffusion between neighboring secondary branches whose radii are

different [8–11]. Thus, remelting/resolidification processes on the thinner/thicker secondary dendrite arms can be witnessed, which can influence the following mechanical properties of structures [8,9]. In addition, there always exists a melt concentration gradient by imposed temperature gradient during directional solidification [12,13]. Thus, solute diffusion can also be induced by this melt concentration, and the remelting/resolidification process by this melt concentration occurs [14–16]. This process is always assumed to be controlled by the temperature gradient zone melting (TGZM) [17–19], and it is also called dendrite migration in some literatures [14–18].

Although the analyses on the remelting/

resolidification process have been carried out in a number of studies discussed above, the role of the diffusionless phase transitions in this remelting/resolidification process has long been neglected. During past decades, more attention has been paid on the diffusionless phase transitions [20–22]. Among them, the hexagonal–orthorhombic (HO) transformation [20,21] appears to be common in a series of alloy systems like Ti–Al–Nb alloy [22]. The only research which correlated the HO transformation with coarsening process confirmed the influence of the HO transformation [23].

In recent decades, the dendrite growth of many industrially important peritectic alloys featured by peritectic reaction $L+\alpha\rightarrow\beta$ has been witnessed, like Fe–Ni, Ti–Al and Cu–Sn [24–26]. The restriction of the coarsening process by the G–T effect was confirmed during peritectic solidification [27]. Besides, the TGZM effect has been proven to not only reduce the interdendritic microsegregation [28] but also accelerate the remelting/resolidification process [29]. Thus, the previous analysis on dendrite growth during peritectic solidification has demonstrated its particularity originated from peritectic reaction. However, the influence of the HO transformation has less been analyzed during peritectic solidification. It has been confirmed that a HO transformation from β -Ni₃Sn₂ phase (hexagonal) to α' -Ni₃Sn₂ phase (orthorhombic) occurred during solidification of Sn–Ni peritectic system [30–32]. So, the occurrence of this HO transformation in Sn–Ni peritectic alloy should be clarified. Besides, the dendrite morphology can be changed if the HO transformation happens, which will lead to the variation of the diffusion distance for both effects. To better understand the diffusion-controlled remelting/resolidification process in peritectic system in the presence of the HO transformation, the present work aims to describe this process in a Sn–30at.%Ni peritectic alloy. The superiority of specific surface (S_V) [8] as compared with other parameters such as λ_2 in characterizing the dendritic structure has been confirmed [8,33–35]. Thus, remelting/resolidification process will be described through S_V in this study.

In the present work, the experimental observation on the morphology features of the TGZM effect, the G–T effect and the HO phase transformation will be given first. Then, the diffusion-controlled analytical theory on the

remelting/resolidification process in consideration of the HO phase transformation will be proposed. After that, the influence of the HO phase transformation on this remelting/resolidification process in a Sn–Ni peritectic alloy will be clarified through the examination on both the theoretical prediction and experimental results.

2 Experimental

The as-cast Sn–30at.%Ni alloy was obtained through induction melting method using nickel and tin with purity of 99.9%. Then, the rods of 3 mm in diameter and 110 mm in length were cut from the ingot. The rod was firstly placed into a Al₂O₃ tube, and the temperature of the rod was raised to 1150 °C. When the rod was completely melted, the sample was kept stationary in the Bridgman-type furnace for 30 min. After that, the directional growth of the rods was performed at different growth velocities: 5, 10, 20 and 40 $\mu\text{m/s}$. Finally, the tube was quenched into liquid Ga–In–Sn alloy when the growth distance was 50 mm. The temperature gradient close to the solid/liquid interface could be deduced from PtRh30–PtRh6 temperature profiles, which was approximately 42 K/mm. The samples were longitudinally sectioned, polished for further analysis by scanning electron microscopy (SEM (Quanta–200)).

The surface area per unit volume S_V was measured in different transverse sections of the rod by $S_V=S/V=\Sigma l/\Sigma A$ [8]. Here, the total area of the dendrites in the transverse section S was obtained by successively polishing down through a dendrite and measuring the length of its peripheral contour l , in each step. The dendrite volume V was measured by $V=\Sigma A \cdot d$, where A is the area of the dendrites on the transverse section and d is the polish depth. The values of l and A were measured using image analysis software Olycia 3.0.

3 Results

The Sn–30at.%Ni alloy experiences three reactions in equilibrium solidification [31]: (1) $T_L=960\text{ }^\circ\text{C}$: $L\rightarrow\text{Ni}_3\text{Sn}_2$; (2) $T_P=798\text{ }^\circ\text{C}$: $L+\text{Ni}_3\text{Sn}_2\rightarrow\text{Ni}_3\text{Sn}_4$; (3) $T_E=231.15\text{ }^\circ\text{C}$, $L\rightarrow\text{Ni}_3\text{Sn}_4+\text{Sn}$. The typical dendrite morphology of the Sn–30at.%Ni alloy is shown in Fig. 1. According to the EDS result, the dark grey phase represents

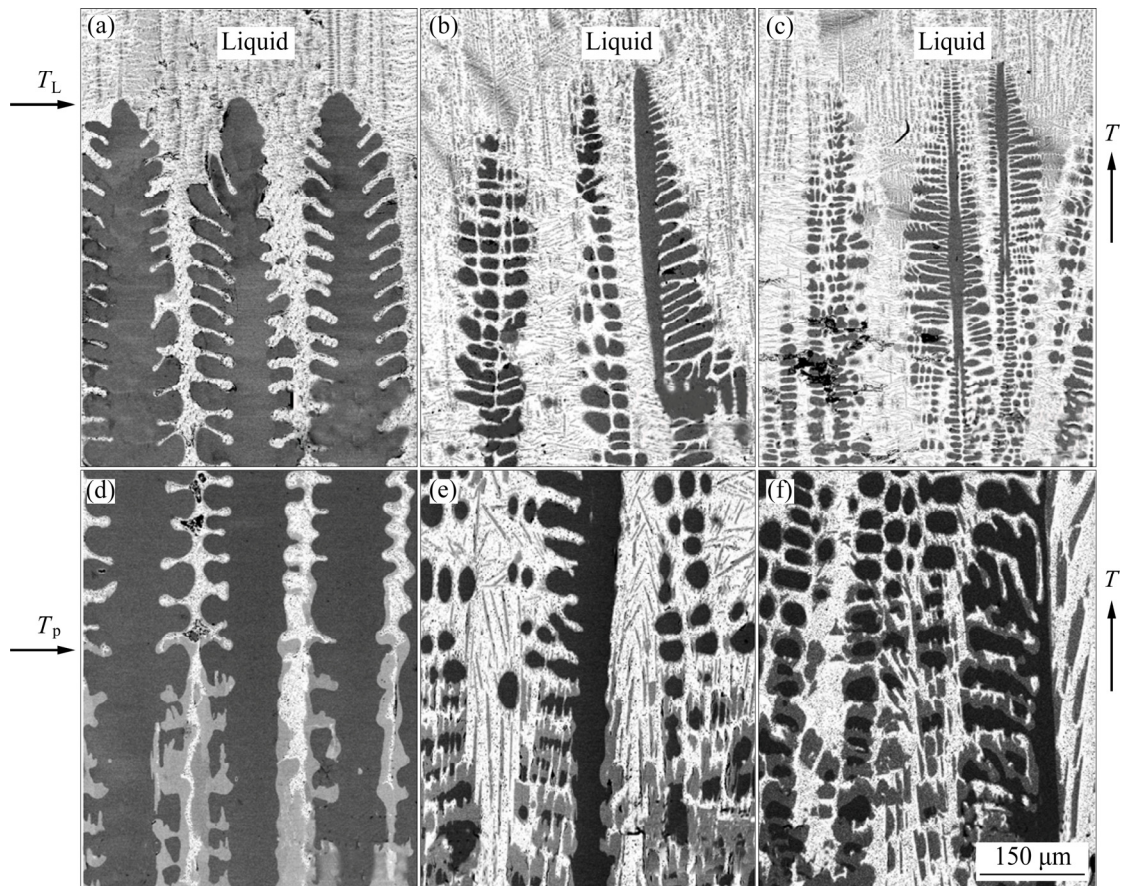


Fig. 1 Microstructures of directionally solidified Sn-30at.%Ni peritectic alloys at quenched solid/liquid interface (a–c) and peritectic interface (d–f): (a, d) 5 $\mu\text{m/s}$; (b, e) 20 $\mu\text{m/s}$; (c, f) 40 $\mu\text{m/s}$

the primary Ni_3Sn_2 phase, and the light grey one is the peritectic Ni_3Sn_4 phase. The white phase is the remaining liquid phase [28,33]. The different radii of the neighboring secondary dendrite arms can be found, indicating the existence of the G–T effect. Furthermore, the examination on Figs. 1(d–f) shows that peritectic Ni_3Sn_4 phase only encloses the higher edge of the secondary branch, which can be confirmed to be characteristic of the TGZM effect during peritectic solidification [15,29]. Thus, how can the TGZM and G–T effects influence the dendrite morphology should be illuminated.

Besides, it is noteworthy from Fig. 1 that the intersection angle (θ) between the primary dendrite stem and secondary branch from it gradually increases from about $\pi/3$ to nearly $\pi/2$ as directional solidification proceeds. Although this phenomenon can be found in every growth velocity, it is most obvious at the lowest growth velocity of 5 $\mu\text{m/s}$ in Fig. 1(a). Since the growth conditions of each controlled directional solidification experiment are steady, whether the variation of θ with solidification

time occurs should be investigated. Owing to the reason that there exists no difference in the morphologies of the primary Ni_3Sn_2 and peritectic Ni_3Sn_4 phases, the interesting variation of θ cannot be related to peritectic reaction. Therefore, the possible reason for the variation of θ with solidification time should be attributed to the phase transformation of primary Ni_3Sn_2 phase. According to the available crystal structure data of this Ni_3Sn_2 phase [30–32], Ni_3Sn_2 high-temperature phase has hexagonal structure, and Ni_3Sn_2 low-temperature phase has orthorhombic structure [32].

If the solid phase has a hexagonal structure, the secondary branch of it always has θ of $\pi/3$. In addition, θ is $\pi/2$ for a solid phase which has a orthorhombic structure. Thus, it can be concluded that the different structures of Ni_3Sn_2 phase at different positions (temperatures) can lead to the variation in θ . Furthermore, it should be noted that since the growth velocities in this work are not high, the peritectic transformation can be clearly observed. However, the peritectic solidification

might be obviously restricted in the case of higher cooling rates and/or deeper undercooling due to solute trapping, solute drag, etc. [27].

The remelting/resolidification processes by the capillary driven G–T effect [8–11] and the temperature gradient induced TGZM effect [14–20] have been confirmed to be closely related to the dendrite morphology. This indicates that this process is influenced by the morphology of secondary branch. The distance between the neighbouring secondary branches is the actual diffusion distance for both effects. The variation of θ with solidification time by the HO phase transformation can result in the change in both the morphology of secondary dendrite arm and the distance between neighbouring secondary branches. Thus, HO phase transformation undoubtedly plays important role in remelting/resolidification process.

4 Discussion

4.1 Analytical model

The schematic representation of dendrite morphology is illustrated in Fig. 2, and the different radii at different local positions of dendrite structure are given. It can be found from Fig. 2 that five radii are mentioned here: the radius of the primary stem R_1 , the tip radius of secondary branch R_2 , the root radius of secondary branch R_{root} , and the root radii of the concave necks, R_3 , and R_4 . In this work, the temperatures of the different parts of the dendrite structures are also given. The definitions of these temperatures in this work when θ equals to $\pi/2$ are

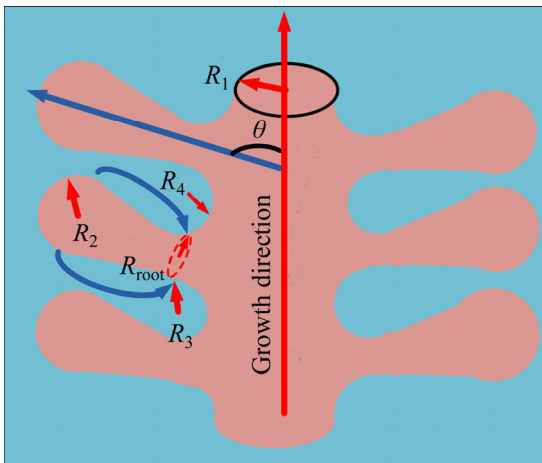


Fig. 2 Schematic presentation of dendrite morphology to identify different radii at different local positions

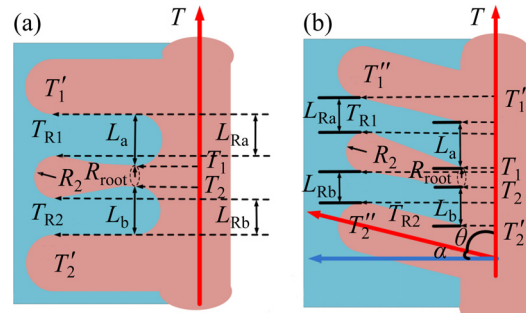


Fig. 3 Definitions of temperatures at different locations of secondary dendrite arms in the present work: (a) $\theta = \pi/2$; (b) $\theta < \pi/2$

given in Fig. 3(a), and the definitions of these temperatures when θ is smaller than $\pi/2$ are shown in Fig. 3(b). If the HO transformation occurs, the situation is more complex. As shown in Fig. 3(b), T_1' and T_2'' are the temperatures at the back/front edges of the tip of thicker ones.

4.2 Comparison between influence of TGZM and G–T effects

Since both the TGZM and G–T effects play significant roles in the remelting/resolidification process, the relative importance between them should be illuminated first. By comparing with the previous coarsening models [8–11], a thinner secondary branch is assumed to be located between two thicker ones in Figs. 4–7. The intersection angle on this thinner secondary branch is defined to be smaller than $\pi/2$. This distribution of the thicker and thinner secondary branch is reasonable since the influences of these two effects on the thinner secondary branch are not always the same. The TGZM effect leads to the remelting/resolidification

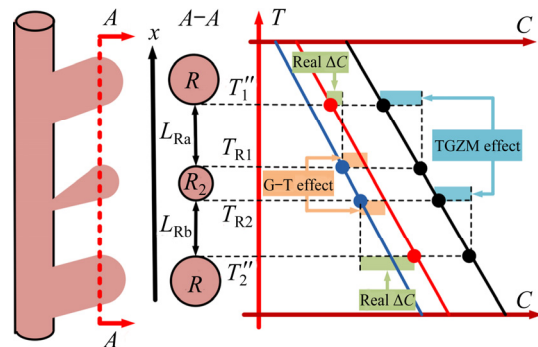


Fig. 4 Illustration of comparison between influence of TGZM and G–T effects on remelting/resolidification process at tip of secondary dendrite arm in Stage I during directional solidification of peritectic alloy

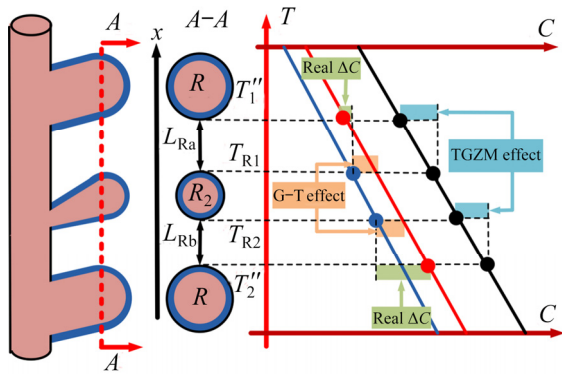


Fig. 5 Illustration of comparison between influence of TGZM and G-T effects on remelting/resolidification process at tip of secondary dendrite arm in Stage II during directional solidification of peritectic alloy

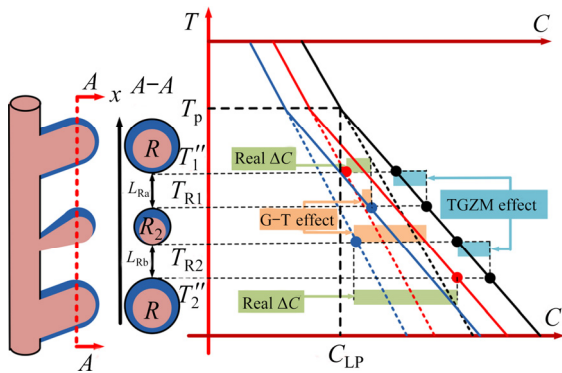


Fig. 6 Illustration of comparison between influence of TGZM and G-T effects on remelting/resolidification process at tip of secondary dendrite arm in Stage III during directional solidification of peritectic alloy

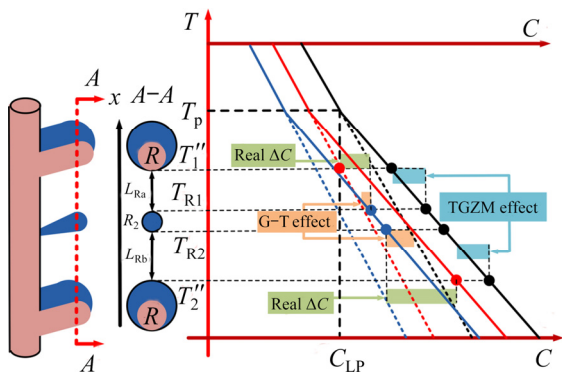


Fig. 7 Illustration of comparison between influence of TGZM and G-T effects on remelting/resolidification process at tip of secondary dendrite arm in Stage IV during directional solidification of peritectic alloy

process at the back/front edges. However, the remelting process induced by the G-T effect occurs at both the back and front edges of the thinner secondary branch. Thus, the proposed morphology

is appropriate. Furthermore, the solute fluxes induced by both effects are assumed to be independent.

Based on the experimental results, as shown in Figs. 4–7, the remelting/resolidification process consists of four stages. In Fig. 4, only primary α phase participates in Stage I above T_p . From the A-A view in Fig. 4, the circles represent the tips of these secondary branches in their radial direction. The straight lines in Fig. 4 are the liquidus of α phase. Here, the black line (electronic version) shows the equilibrium liquidus line when the curvature undercooling is not taken into account. When the curvature undercooling [9] is taken into consideration, the red (blue) line is the liquidus line if the radius is R (R_2). Figure 4 clearly shows that the melt difference ΔC by the TGZM effect is larger than that by the G-T effect at both T_{R1} and T_{R2} . This indicates that the G-T effect is less important as compared with the TGZM effect on both edges. As a matter of fact, the real ΔC on the front edge is the difference between ΔC by both effects at T_{R1} . Simultaneously, the real ΔC on the back edge is the sum of ΔC by both effects at T_{R2} . Therefore, the real ΔC at T_{R2} is larger than that at T_{R1} .

Stage II initiates when the temperature is below T_p , and only peritectic β phase is considered in this stage. Figure 5 confirms that the melt difference ΔC by the G-T effect is still smaller than that by the TGZM effect at both T_{R1} and T_{R2} . This indicates that the TGZM effect is more important than the G-T effect on both edges in Stage II. Since it has been confirmed [30] that the remelting velocity at T_{R2} was larger than the resolidification velocity at T_{R1} , R_2 gradually decreases. Furthermore, the β phase at T_{R2} should completely remelt first, and then as shown in Fig. 6, Stage III takes place. In this case, peritectic β phase appears at T_2'' and primary α phase appears at T_{R2} . The dashed lines in Fig. 6 represent the liquidus lines of primary α phase below T_p , and they are assumed to be the extension of the oblique straight lines above T_p . As mentioned above, the remelting velocity at T_{R2} is larger than the resolidification velocity at T_{R1} . Therefore, Stage III is finished when the β phase at T_1'' completely remelts. In this case, as displayed in Fig. 7, peritectic β phase appears at T_1'' and primary α phase appears at T_{R1} . The whole remelting/resolidification process is finished when this thinner

secondary branch finally disappears.

4.3 Analytical model on tip radius of secondary arm

4.3.1 Stage I

As shown in Fig. 2, the undercooling due to curvature effect is [11]

$$\Delta T_R = \Gamma \left[\left(\frac{1}{R_{\text{root}}} - \frac{1}{R_3} \right) - \frac{1}{R_2} \right] \quad (1a)$$

Thus, while the actual temperature at the root of the thinner secondary branch is lower than that in equilibrium condition, the actual temperature at the tip is higher than it. It can be obtained from Fig. 4:

$$T_1'' = T_\alpha + m_1^\alpha C_1^{\alpha, T_1''} - \frac{\Gamma}{R} \quad (1b)$$

$$T_{R1} = T_\alpha + m_1^\alpha C_1^{\alpha, T_{R1}} + \Gamma \left[\left(\frac{1}{R_{\text{root}}} - \frac{1}{R_3} \right) - \frac{1}{R_2} \right] \quad (1c)$$

where Γ is the Gibbs–Thomson coefficient; m_1^α is the liquidus slope of primary α phase; $C_1^{\alpha, T_1''}$ and $C_1^{\alpha, T_{R1}}$ are the melt concentrations at T_1'' and T_{R1} , respectively.

Since a temperature gradient is imposed on the interdendritic liquid layer, it can be obtained that:

$$T_1'' = T_{R1} + GL_{Ra} \quad (2)$$

where G is the temperature gradient during directional solidification.

It can be obtained from Eqs. (1) and (2) that:

$$C_1^{\alpha, T_{R1}} - C_1^{\alpha, T_1''} = -\frac{\Gamma}{m_1^\alpha} \left[\left(\frac{1}{R_{\text{root}}} - \frac{1}{R_3} \right) - \frac{1}{R_2} - \frac{1}{R} \right] - \frac{GL_{Ra}}{m_1^\alpha} \quad (3)$$

Based on Fick’s First Law, the solute diffusion flux between T_1'' and T_{R1} can be expressed as

$$J_1 = D_L \frac{C_1^{\alpha, T_{R1}} - C_1^{\alpha, T_1''}}{L_{Ra}} = -\frac{D_L}{m_1^\alpha L_{Ra}} \left[\Gamma \left[\left(\frac{1}{R_{\text{root}}} - \frac{1}{R_3} \right) - \frac{1}{R_2} - \frac{1}{R} \right] + GL_{Ra} \right] \quad (4)$$

where D_L is the solute diffusion coefficient of melt. And for a small displacement dR_2 at T_1'' , there is

$$J_2 = C_1^{\alpha, T_{R1}} (1 - k_\alpha) \frac{dR_2}{dt} \Big|_{T_{R1}} \quad (5)$$

$$J_1 = J_2 \quad (6)$$

$$\left\{ \begin{aligned} \frac{dR_2}{dt} \Big|_{T_{R1}} &= -\frac{D_L}{m_1^\alpha C_1^{\alpha, T_{R1}} (1 - k_\alpha) L_{Ra}} \cdot \\ &\left[\Gamma \left[\left(\frac{1}{R_{\text{root}}} - \frac{1}{R_3} \right) - \frac{1}{R_2} - \frac{1}{R} \right] + GL_{Ra} \right] \\ L_{Ra} &= L_a + (R_2 - R) \cos \theta \end{aligned} \right. \quad (7)$$

Similarly, at the back edge, there is

$$\left\{ \begin{aligned} \frac{dR_2}{dt} \Big|_{T_{R2}} &= -\frac{D_L}{m_1^\alpha C_1^{\alpha, T_{R2}} (1 - k_\alpha) L_{Rb}} \cdot \\ &\left[\Gamma \left[\left(\frac{1}{R_{\text{root}}} - \frac{1}{R_3} \right) - \frac{1}{R_2} - \frac{1}{R} \right] - GL_{Rb} \right] \\ L_{Rb} &= L_b + (R - R_2) \cos \theta \end{aligned} \right. \quad (8)$$

where $C_1^{\alpha, T_{R1}}$ and $C_1^{\alpha, T_{R2}}$ are melt concentrations at T_{R1} and T_{R2} , respectively. The relation between $C_1^{\alpha, T_{R1}}$ and $C_1^{\alpha, T_{R2}}$ is

$$C_1^{\alpha, T_{R1}} - C_1^{\alpha, T_{R2}} = \frac{G}{m_1^\alpha} \cdot (2R_2) \quad (9)$$

$$\frac{dR_2}{dt} \Big|_{\text{Stage I}} = \frac{1}{2} \left(\frac{dR_2}{dt} \Big|_{T_{R1}} + \frac{dR_2}{dt} \Big|_{T_{R2}} \right) \quad (10)$$

The comparison between Eqs. (7a) and (8a) shows that the remelting velocity at T_{R2} is smaller than the resolidification velocity at T_{R1} . This seems to be contradictory to the previous analysis in Section 4.2, and this can be attributed to the complex morphology of the secondary branch. Although the solute diffusion between neighbouring secondary dendrite can lead to remelting of the tip of the thinner secondary branch, the diffusion between the tip and root of the same secondary branch plays a more important role according to our analysis. As a matter of fact, Fig. 1 shows the gradual increase of the tip radius of the thinner secondary branch. Furthermore, it can also be found that the solute concentration difference ΔC by the G–T effect at the tip of secondary branch is smaller as compared with that at the root of secondary branch. This is consistent with the fact that the difference in radius between the tip of the thinner secondary branch and its neighboring thicker ones is smaller than that at the root of the thinner secondary branch. As illustrated in Eqs. (7a) and (8a), the dependence of R_2 on the root radius R_{root}

shows that the variation of R_2 during the remelting/resolidification process should also be identified.

4.3.2 Stage II

As shown in Fig. 5, resolidification velocity at T_{R1} can be given as

$$\left\{ \begin{aligned} \left. \frac{dR_2}{dt} \right|_{T_{R1}} &= -\frac{D_L}{m_1^\beta C_1^{\beta,T_{R1}} (1-k_\beta) L_{Ra}} \cdot \\ &\left[\Gamma \left[\left(\frac{1}{R_{root}} - \frac{1}{R_3} \right) - \frac{1}{R_2} - \frac{1}{R} \right] + GL_{Ra} \right] \\ L_{Ra} &= L_a + (R_2 - R) \cos \theta \end{aligned} \right. \quad (11)$$

The remelting velocity of β phase at T_{R2} can be given by

$$\left\{ \begin{aligned} \left. \frac{dR_2}{dt} \right|_{T_{R2}} &= -\frac{D_L}{m_1^\beta C_1^{\beta,T_{R2}} (1-k_\beta) L_{Rb}} \cdot \\ &\left[\Gamma \left[\left(\frac{1}{R_{root}} - \frac{1}{R_3} \right) - \frac{1}{R_2} - \frac{1}{R} \right] - GL_{Rb} \right] \\ L_{Rb} &= L_b + (R - R_2) \cos \theta \end{aligned} \right. \quad (12)$$

where m_1^β is the liquidus slope of peritectic β phase, $C_1^{\beta,T_{R1}}$ and $C_1^{\beta,T_{R2}}$ are the melt concentrations at T_{R1} and T_{R2} , respectively. The relation between $C_1^{\beta,T_{R1}}$ and $C_1^{\beta,T_{R2}}$ is

$$C_1^{\beta,T_{R1}} - C_1^{\beta,T_{R2}} = \frac{G}{m_1^\beta} \cdot (2R_2) \quad (13)$$

$$\left. \frac{dR_2}{dt} \right|_{Stage II} = \frac{1}{2} \left(\left. \frac{dR_2}{dt} \right|_{T_{R1}} + \left. \frac{dR_2}{dt} \right|_{T_{R2}} \right) \quad (14)$$

Similar to Stage I, as the remelting velocity at T_{R2} is larger than the resolidification velocity at T_{R1} , β phase previously formed at T_{R2} remelts completely, and then Stage III initiates.

4.3.3 Stage III

As exhibited in Fig. 6, it can be obtained that

$$\left\{ \begin{aligned} \left. \frac{dR_2}{dt} \right|_{T_{R1}} &= -\frac{D_L}{m_1^\beta C_1^{\beta,T_{R1}} (1-k_\beta) L_{Ra}} \cdot \\ &\left[\Gamma \left[\left(\frac{1}{R_{root}} - \frac{1}{R_3} \right) - \frac{1}{R_2} - \frac{1}{R} \right] + GL_{Ra} \right] \\ L_{Ra} &= L_a + (R_2 - R) \cos \theta \end{aligned} \right. \quad (15)$$

where $C_1^{\beta,T_{R1}}$ is the melt concentration at T_{R1} .

At T_{R2} , one has

$$T_2'' = T_\beta + m_1^\beta C_1^{\beta,T_2''} \quad (16a)$$

$$T_{R2} = T_\alpha + m_1^\alpha C_1^{\alpha,T_{R2}} + \Gamma \left[\left(\frac{1}{R_{root}} - \frac{1}{R_3} \right) - \frac{1}{R_2} - \frac{1}{R} \right] \quad (16b)$$

Since a temperature gradient is imposed on the interdendritic liquid layer, it can be obtained that

$$T_{R2} = T_2'' + GL_{Rb} \quad (16c)$$

It can be obtained from Eqs. (16a) and (16c) that

$$C_1^{\beta,T_2''} - C_1^{\alpha,T_{R2}} = \frac{1}{m_1^\beta} [(m_1^\beta - m_1^\alpha) (C_{LP} - C_1^{\alpha,T_{R2}}) + \Gamma \left[\left(\frac{1}{R_{root}} - \frac{1}{R_3} \right) - \frac{1}{R_2} - \frac{1}{R} \right] - GL_{Rb}] \quad (17)$$

Similarly to Eq. (5), at the temperature ranging from T_{R2} to T_2'' , there is

$$J = D_L \frac{C_1^{\beta,T_2''} - C_1^{\alpha,T_{R2}}}{L_{Rb}} \quad (18)$$

By applying a mass balance at the α /liquid interface, there is

$$J = D_L \frac{C_1^{\beta,T_2''} - C_1^{\alpha,T_{R2}}}{L_{Rb}} = \frac{dR_2}{dt} (C_1^{\alpha,T_{R2}} - C_\alpha^{l,T_{R2}}) \quad (19)$$

From Eqs. (18) and (19), the remelting velocity of α phase at T_{R2} is

$$\left\{ \begin{aligned} \left. \frac{dR_2}{dt} \right|_{T_{R2}} &= \frac{D_L}{m_1^\beta C_1^{\alpha,T_{R2}} L_{Rb} (k_\alpha - 1)} \cdot \\ &\left[\Gamma \left(\frac{1}{R_{root}} - \frac{1}{R_3} - \frac{1}{R_2} - \frac{1}{R} \right) - GL_{Rb} + \right. \\ &\left. (m_1^\beta - m_1^\alpha) (C_{LP} - C_1^{\alpha,T_{R2}}) \right] \\ L_{Rb} &= L_b + (R - R_2) \cos \theta \end{aligned} \right. \quad (20)$$

The relation between $C_1^{\beta,T_{R1}}$ in Eq. (15a) and $C_1^{\alpha,T_{R2}}$ is

$$C_1^{\alpha,T_{R2}} - C_1^{\beta,T_{R1}} = \frac{T_P - T_{R1}}{m_1^\beta} - \frac{T_P - T_{R2}}{m_1^\alpha} = (T_P - T_{R1}) \left(\frac{1}{m_1^\beta} - \frac{1}{m_1^\alpha} \right) - \frac{G}{m_1^\alpha} \cdot (2R_2) \quad (21)$$

$$\left. \frac{dR_2}{dt} \right|_{\text{Stage III}} = \frac{1}{2} \left(\left. \frac{dR_2}{dt} \right|_{T_{R1}} + \left. \frac{dR_2}{dt} \right|_{T_{R2}} \right) \quad (22)$$

4.3.3 Stage IV

In this case, the resolidification velocity of peritectic β phase at T_{R1} in Stage IV is

$$\left. \frac{dR_2}{dt} \right|_{T_{R1}} = \frac{D_L}{m_1^\alpha C_1^{\beta, T_{R1}} (1 - k_\beta) L_{Ra}} \cdot \left[(m_1^\beta - m_1^\alpha) (C_{LP} - C_1^{\beta, T_{R1}}) + \Gamma \left[\left(\frac{1}{R_{\text{root}}} - \frac{1}{R_3} \right) - \frac{1}{R_2} - \frac{1}{R} \right] - GL_{Ra} \right] \quad (23)$$

$$L_{Ra} = L_a + (R_2 - R) \cos \theta$$

The remelting velocity of β phase at T_{R2} is

$$\left. \frac{dR_2}{dt} \right|_{T_{R2}} = - \frac{D_L}{m_1^\beta C_1^{\beta, T_{R2}} (1 - k_\beta) L_{Rb}} \cdot \left\{ \Gamma \left[\left(\frac{1}{R_{\text{root}}} - \frac{1}{R_3} \right) - \frac{1}{R_2} - \frac{1}{R} \right] - GL_{Rb} \right\} \quad (24)$$

$$L_{Rb} = L_b + (R - R_2) \cos \theta$$

Here, the relation between $C_1^{\beta, T_{R1}}$ and $C_1^{\beta, T_{R2}}$ is

$$C_1^{\beta, T_{R1}} - C_1^{\beta, T_{R2}} = \frac{G}{m_1^\beta} \cdot (2R_2) \quad (25)$$

$$\left. \frac{dR_2}{dt} \right|_{\text{StageIV}} = \frac{1}{2} \left(\left. \frac{dR_2}{dt} \right|_{T_{R1}} + \left. \frac{dR_2}{dt} \right|_{T_{R2}} \right) \quad (26)$$

4.4 Dependence of θ on solidification time

To better understand the influence of the HO phase transformation on remelting/resolidification process, the dependence of θ on solidification time is given in Fig. 8. Besides, according to above analysis, the dependence of $\cos \theta$ on solidification time which is closely related to the remelting/resolidification velocity is also presented in Fig. 9. Examination on Figs. 8 and 9 confirms the clear dependence of both θ and $\cos \theta$ on solidification time at each growth velocity. Besides, the influence of the growth velocity on θ and $\cos \theta$ can also be found. On the one hand, the initial value of the angle (θ_0) in the vicinity of the tip of primary dendrite stem increases with increasing growth velocity: from 69° at $5 \mu\text{m/s}$ to 83° at $40 \mu\text{m/s}$. On the other hand, the range of θ and $\cos \theta$ gradually

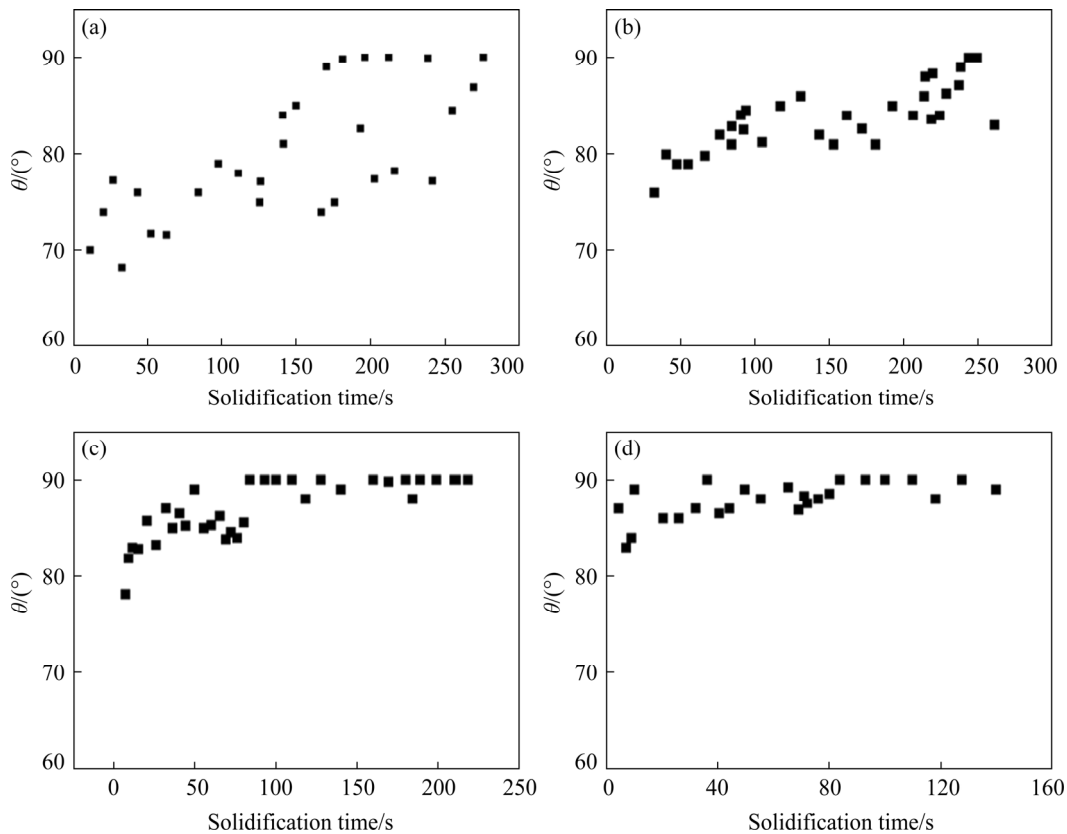


Fig. 8 Dependence of intersection angle (θ) on solidification time at different growth velocities: (a) $5 \mu\text{m/s}$; (b) $10 \mu\text{m/s}$; (c) $20 \mu\text{m/s}$; (d) $40 \mu\text{m/s}$

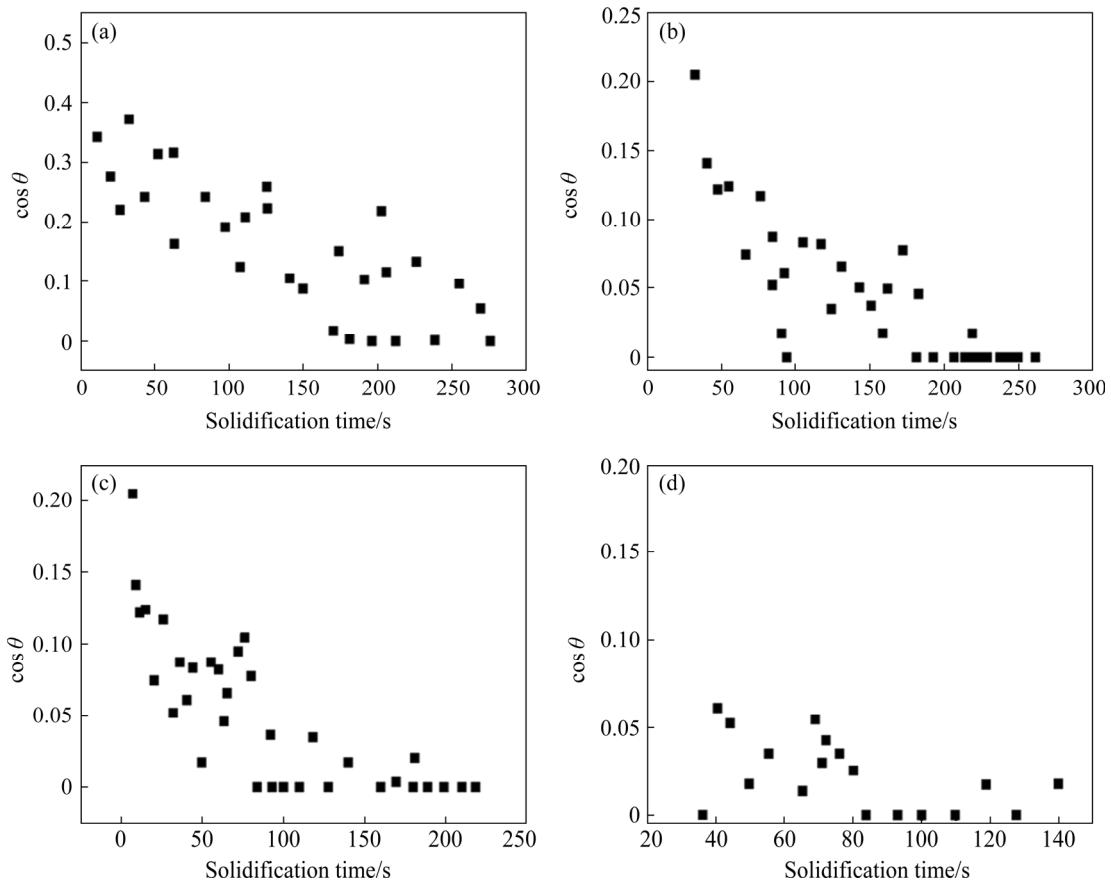


Fig. 9 Dependence of $\cos \theta$ on solidification time at different growth velocities: (a) $5 \mu\text{m/s}$; (b) $10 \mu\text{m/s}$; (c) $20 \mu\text{m/s}$; (d) $40 \mu\text{m/s}$

decreases as the growth velocity increases. The dependence of both θ and $\cos \theta$ on the growth velocity can be attributed to the driving force of the HO phase transformation [21–26], which is accelerated by the larger undercooling at larger growth velocity. Furthermore, the ever-changing image of θ throughout the directional solidification process is seen before it reaches $\pi/2$. Thus, it can be inferred from the expressions of the remelting/resolidification rates that the real remelting/resolidification process keeps varying as directional solidification proceeds.

4.5 Influence of θ on remelting/resolidification process

As discussed above, the secondary dendrite arms are not strictly perpendicular to the primary dendrite stems after the HO phase transformation. The variation of θ by the HO phase transformation definitely changes the diffusion distances of remelting/resolidification process by both the TGZM and G-T effects. Taking Stage I for example, according to Eq. (7b), the diffusion distance of the resolidification process on the front edge of the tip

of the thinner secondary branch (L_{Ra}) increases with the increase of θ ($\pi/3 < \theta < \pi/2$). As a result, the resolidification rate gradually decreases. Similarly, it can be found through Eq. (8b) that the diffusion distance of the remelting process on the back edge (L_{Rb}) also increases simultaneously with the increase of θ , leading to the decrease of the remelting rate as directional solidification proceeds. In a word, the remelting/resolidification process is restricted if the HO phase transformation occurs during solidification.

To better display the influence of the HO phase transformation on the remelting/resolidification process, the theoretical prediction through the present model in which the HO phase transformation is not taken into consideration ($\theta = \pi/2$) is presented in Fig. 10. The calculation procedures have been shown in detail in a previous work [35]. The dependence of $\cos \theta$ on solidification time is given through the polynomial approximation of experimental results. Besides, the present theoretical prediction when the HO phase transformation is considered is compared with the experimental measurement in Fig. 11. The

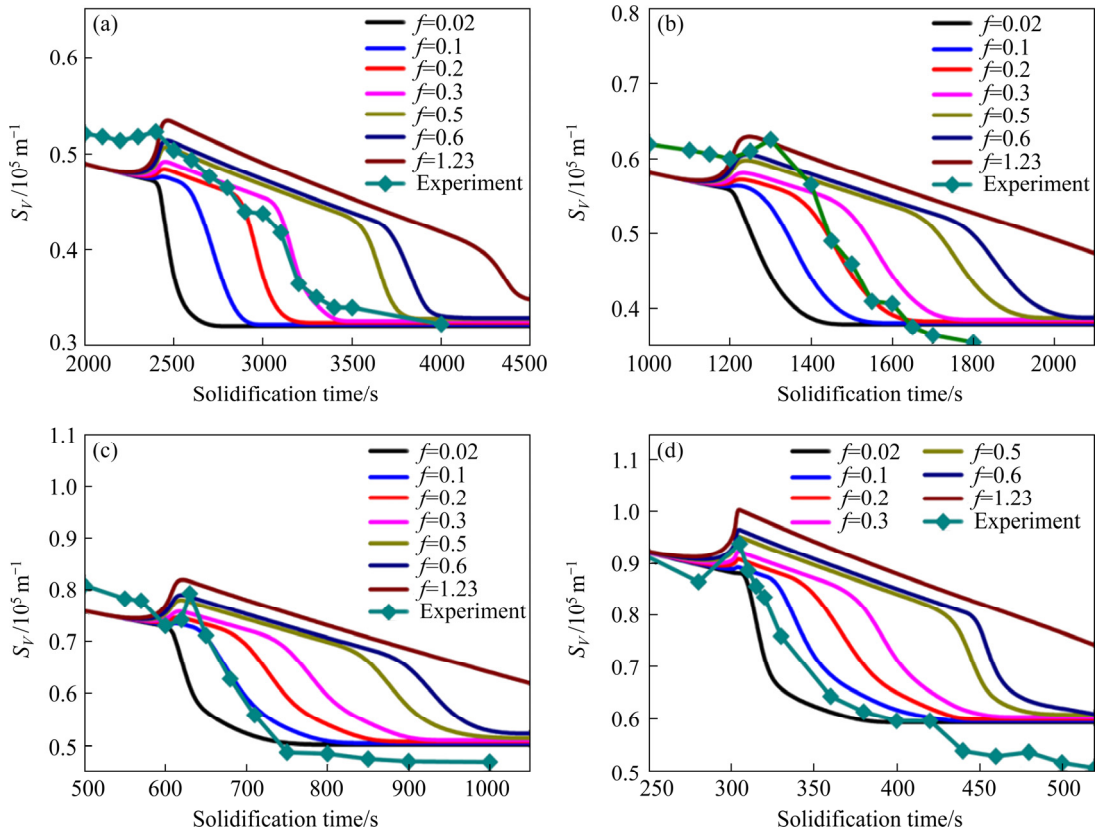


Fig. 10 Comparison between theoretical prediction in which HO phase transformation is not taken into consideration ($\theta=\pi/2$) and experimental measurement at different growth velocities: (a) $5 \mu\text{m/s}$; (b) $10 \mu\text{m/s}$; (c) $20 \mu\text{m/s}$; (d) $40 \mu\text{m/s}$

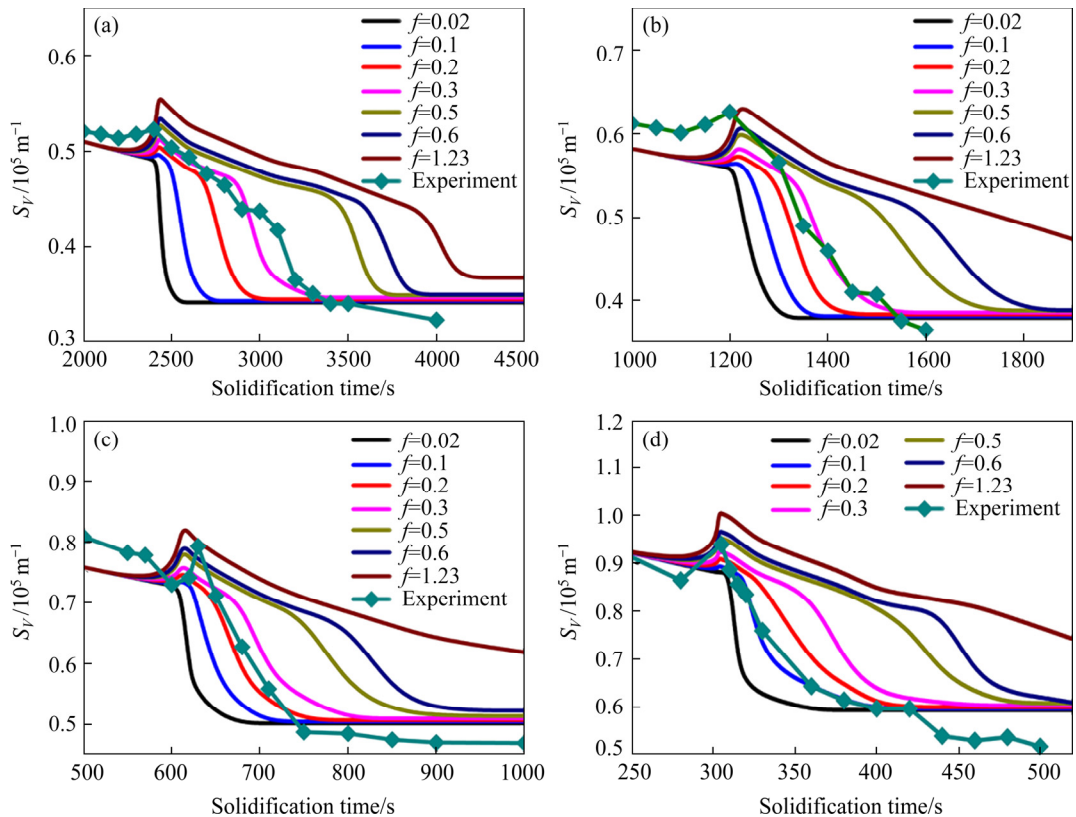


Fig. 11 Comparison between theoretical prediction in which HO phase transformation is taken into consideration ($\theta<\pi/2$) and experimental measurement at different growth velocities: (a) $5 \mu\text{m/s}$; (b) $10 \mu\text{m/s}$; (c) $20 \mu\text{m/s}$; (d) $40 \mu\text{m/s}$

comparison between Figs.10 and 11 shows the gradual decrease of the remelting/resolidification rates during directional solidification. This means that the remelting/resolidification process is underestimated in previous researches [15,30] if the HO phase transformation is neglected. In addition, the present theoretical prediction also shows the gradual decrease of the slope of the prediction curves during solidification. This further confirms the restriction on this process in the presence of the HO transformation, proving the validity and reliability of the present model.

Based on the analyses above, four different reasons are involved during the remelting/resolidification process in Sn–Ni peritectic system: the G–T effect, TGZM effect, peritectic reaction and the HO phase transformation. Since their influences are different, even contradictory, their combined influences are more complex. Although the G–T effect is retarded during peritectic solidification, the combined influences of both effects and peritectic reaction in turn accelerate the coarsening process [30]. The influence of the HO phase transformation mainly lies in changing the morphology of secondary dendrite arm, thus altering the solute diffusion within liquid layers between secondary branches.

5 Conclusions

(1) The intersection angle between the primary dendrite stem and secondary branch (θ) is observed to increase from $\pi/3$ to $\pi/2$, which is confirmed to be the morphology feature of the HO phase transformation from β -Ni₃Sn₂ phase (hexagonal) to α' -Ni₃Sn₂ phase (orthorhombic).

(2) A diffusion-based analytical model is established to describe remelting/resolidification process in the presence of the HO phase transformation. The theoretical prediction confirms that this process is restricted by the HO phase transformation during peritectic solidification since it can change the diffusion distance.

(3) The present theoretical prediction shows that the slope of the prediction curves always changes since θ continues varying during the remelting/resolidification process.

Acknowledgments

The authors acknowledge the support from

the Natural Science Foundation of China (No. 51871118), Open Project of Key Laboratory for Magnetism and Magnetic Materials of the Ministry of Education, Lanzhou University, China (No. LZUMMM2021005), the Science and Technology Project of Lanzhou City, China (No. 2019-1-30), and State Key Laboratory of Special Rare Metal Materials, China (No. SKL2020K003).

References

- [1] YANG Yong, FENG He-ping, WANG Qi, CHEN Rui-run, GUO Jing-jie, DING Hong-sheng, SU Yan-qing. Improvement of microstructure and mechanical properties of TiAl–Nb alloy by adding Fe element [J]. Transactions of Nonferrous Metals Society of China, 2020, 30: 1315–1324.
- [2] TRIVEDI R, KURZ W. Dendritic growth [J]. International Materials Reviews, 1994, 39: 49–74.
- [3] ZHANG Yu, JING Hong-yang, XU Lian-yong, HAN Yong-dian, ZHAO Lei, LI Hai-zhou, TANG Zheng-xin, TONG Tian-wang. Microstructure and grain boundary engineering of a novel Fe–Cr–Ni alloy weldment made with self-developed composition-matched weld filler metal [J]. Transactions of Nonferrous Metals Society of China, 2020, 30: 992–1004.
- [4] LÜ Peng, WANG Hai-peng, WEI Bing-bo. Competitive nucleation and growth between the primary and peritectic phases of rapidly solidifying Ni–Zr hypoperitectic alloy [J]. Metallurgical Materials Transactions A, 2019, 50: 789–803.
- [5] ECHEBARRIA B, KARMA A, GUREVICH S. Onset of sidebranching in directional solidification [J]. Physical Review E, 2010, 81: 021608.
- [6] LÜ Peng, WANG Hai-peng. Effects of undercooling and cooling rate on peritectic phase crystallization within Ni–Zr alloy melt [J]. Metallurgical and Materials Transactions B, 2018, 49: 499–508.
- [7] COUGHLIN J C, KATTAMIS T Z, FLEMINGS M C. Influence of coarsening on dendrite arm spacing of aluminum–copper alloys [J]. Transaction of the Metallurgical Society of AIME, 1967, 239: 1504–1511.
- [8] MARSH S P, GLICKSMAN M E. Overview of geometric effects on coarsening of mushy zones [J]. Metallurgical and Materials Transactions A, 1996, 27: 557–567.
- [9] ZHAO Kang, WU Shuang, JIANG Si-yuan, ZHANG He-zhi, SONG Kai-kai, WANG Ting, XING Hui, ZHANG Li-ming, LI Ke-feng, YANG Lei, WANG Xiao-li, WANG Li. Microstructural refinement and anomalous eutectic structure induced by containerless solidification for high-entropy Fe–Co–Ni–Si–B alloys [J]. Intermetallics, 2020, 122: 106812.
- [10] CHEN M, KATTAMIS T Z. Dendrite coarsening during directional solidification of Al–Cu–Mn alloys [J]. Materials Science and Engineering A, 1998, 247: 239–247.
- [11] LIOTTI E, LUI A, VINCENT R, KUMAR S, GUO Z, CONNOLLEY T, DOLBANYA I P, HART M, ARNBERG L,

- MATHIESEN R H, GRANT P S. A synchrotron X-ray radiography study of dendrite fragmentation induced by a pulsed electromagnetic field in an Al–15Cu alloy [J]. *Acta Materialia*, 2014, 70: 228–239.
- [12] RETTENMAYR M. Melting and remelting phenomena [J]. *International Materials Reviews*, 2009, 54: 1–17.
- [13] PFANN W G. Temperature gradient zone melting [J]. *Transactions of the AIME*, 1955, 203: 961–964.
- [14] ALLEN D J, HUNT J D. Melting during solidification [J]. *Metallurgical and Materials Transactions A*, 1976, 7: 767–770.
- [15] LIU Dong-mei, LI Xin-zhong, SU Yan-qing, PENG Peng, LUO Liang-sun, GUO Jing-jie, FU Heng-zhi. Secondary dendrite arm migration caused by temperature gradient zone melting during peritectic solidification [J]. *Acta Materialia*, 2012, 60: 2679–2688.
- [16] FOURNELLE R A. On the thermodynamic driving force for diffusion-induced grain boundary migration, discontinuous precipitation and liquid film migration in binary alloys [J]. *Materials Science and Engineering A*, 1991, 138: 133–145.
- [17] TANAKA Y, KAJIHARA M. Numerical analysis for migration of interface between liquid and solid phases during reactive diffusion in the binary Cu–Al system [J]. *Materials Science and Engineering A*, 2007, 459: 101–110.
- [18] NGUYEN T H, REINHART G, BUFFET A, SCHENK D T, ANGELINCK NOËL N, JUNG H, BERGEON N, BILLIA B, HÄRTWIG J, BARUCHEL J. In situ and real-time analysis of TGZM phenomena by synchrotron X-ray radiography [J]. *Journal of Crystal Growth*, 2008, 310: 2906–2914.
- [19] PAN Shi-yan, ZHANG Qing-yu, ZHU Ming-fang, RETTENMAYR M. Liquid droplet migration under static and dynamic conditions: Analytical model, phase-field simulation and experiment [J]. *Acta Materialia*, 2015, 86: 229–239.
- [20] CUI Y W, KOYAMA T, OHNUMA I, OIKAWA K, KAINUMA R, ISHIDA K. Simulation of hexagonal–orthorhombic phase transformation in polycrystals [J]. *Acta Materialia*, 2007, 55: 233–241.
- [21] MAMIVAND M, ZAEEM M A, KADIRI H E. Shape memory effect and pseudoelasticity behavior in tetragonal zirconia polycrystals: A phase field study [J]. *International Journal of Plasticity*, 2014, 60: 71–86.
- [22] MURALEEDHARAN K, BANERJEE D, BANERJEE S, LELE S. The α_2 -to- O transformation in Ti–Al–Nb alloys [J]. *Philosophical Magazine A*, 1995, 71: 1011–1036.
- [23] WEN Y H, WANG Y, CHEN L Q. Effect of elastic interaction on the formation of a complex multi-domain microstructural pattern during a coherent hexagonal to orthorhombic transformation [J]. *Acta Materialia*, 1999, 47: 4375–4386.
- [24] KERR H W, KURZ W. Solidification of peritectic alloys [J]. *International Materials Reviews*, 1996, 41: 129–164.
- [25] WANG Shu-jie, WANG Liang, LUO Liang-shun, SU Yan-qing, DONG Fu-yu, GUO Jing-jie, FU Heng-zhi. Stability of remelting and solidification interfaces of triple-phase region during peritectic reaction at lower speed [J]. *Transactions of Nonferrous Metals Society of China*, 2014, 24: 1951–1958.
- [26] PENG Peng, LI Sheng-yuan, ZHENG Wan-chao, LU Li, ZHOU Shu-dong. Macrosegregation and thermosolutal convection-related freckle formation in directionally solidified Sn–Ni peritectic alloy in crucibles of different diameters [J]. *Transactions of Nonferrous Metals Society of China*, 2021, 31: 3096–3104.
- [27] MA D, XU W, NG S C, LI Y. On secondary dendrite arm coarsening in peritectic solidification [J]. *Materials Science and Engineering A*, 2005, 390: 52–62.
- [28] PENG Peng, LI Xin-zhong, SU Yan-qing, GUO Jing-jie, FU Heng-zhi. Microsegregation of peritectic systems in a temperature gradient: Analysis in directionally solidified Sn–36at.%Ni peritectic alloy [J]. *International Journal of Heat and Mass Transfer*, 2016, 94: 488–497.
- [29] PENG Peng, LI Xin-zhong, SU Yan-qing, GUO Jing-jie, FU Heng-zhi. The diffusion-controlled remelting/resolidification process in directionally solidified Sn–Mn peritectic alloy [J]. *International Journal of Heat and Mass Transfer*, 2019, 131: 1129–1137.
- [30] VASSILEV G P, ILOVA K I, GACHON J C. Enthalpies of formation of Ni–Sn compounds [J]. *Thermochimica Acta*, 2006, 447: 106–108.
- [31] SCHMETTERER C, FLANDORFER H, RICHTER W K, SAEED U, KAUFFMAN M, ROUSSEL P, IPSER H. A new investigation of the system Ni–Sn [J]. *Intermetallics*, 2007, 15: 869–884.
- [32] FJELLVAG H, KJEKSHUS A. Structural properties of Co_3Sn_2 , Ni_3Sn_2 and some ternary derivatives [J]. *Acta Chemica Scandinavica*, 1986, 40: 23–30.
- [33] PENG Peng, LI Xin-zhong, LIU Dong-mei, SU Yan-qing, GUO Jing-jie, FU Heng-zhi. Effect of peritectic reaction on dendrite coarsening in directionally solidified Sn–36at.%Ni alloy [J]. *Journal of Materials Science*, 2012, 47: 6108–6117.
- [34] GALENKO P K, JOU D. Rapid solidification as non-ergodic phenomenon [J]. *Physics Reports*, 2019, 818: 1–70.
- [35] JACKSON K A, HUNT J D. Transparent compounds that freeze like metals [J]. *Acta Metallurgica*, 1965, 13: 1212–1215.

六方-正方相变对定向凝固 Sn-Ni 包晶合金中 扩散控制的枝晶演化的影响

彭 鹏^{1,2}, 赵弼洲³, 王甲泰², 裴 兴¹, 刘子杰¹, 甘 露¹, 李升渊¹

1. 兰州大学 材料与能源学院, 兰州 730000;
2. 青海师范大学 物理与电子信息学院, 西宁 753000;
3. 甘肃省中医院, 兰州 730000

摘 要: 在定向凝固 Sn-Ni 包晶合金中发现六方-正方相变, 即自 β -Ni₃Sn₂ (六方) 向 α' -Ni₃Sn₂ (正方) 相的转变。研究表明, 二次枝晶臂上发生由温度梯度区域熔化(TGZM)与吉布斯-汤姆森(G-T)效应引起的重熔/再凝过程。此外, 一次枝晶干与二次分枝间夹角(θ)随凝固过程进行由 $\pi/3$ 增至 $\pi/2$, 这一现象为六方-正方转变的组织特征, 并会改变重熔/再凝过程中的扩散距离。因此, 建立扩散控制唯象模型, 重熔/再凝过程由枝晶的比表面积(S_V)进行表征。模型预测表明, 包晶凝固过程中发生六方-正方相变后可抑制重熔/再凝过程。另外, 预测曲线的斜率变化表明重熔/再凝过程局域速率发生改变。

关键词: 定向凝固; 枝晶凝固; 包晶组织; 吉布斯-汤姆森效应; 温度梯度区域熔化; HO 相变

(Edited by Bing YANG)